Acta Crystallographica Section D
Biological Crystallography
ISSN 0907-4449

Reducing radiation damage in macromolecular crystals at synchrotron sources

Edward A. Stern,[a]* Yizhak Yacoby,[b] Gerald T. Seidler,[a] Kenneth P. Nagle,[a] Micah P. Prange,[a] Adam P. Sorini,[a] John J. Rehr[a] and Andrzej Joachimiak[c]

[a]Physics Department, University of Washington, Seattle, Washington 98195-1560, USA, [b]Racah Institute of Physics, Hebrew University, Jerusalem, Israel, and [c]Center for Mechanistic Biology and Biotechnology, Argonne National Laboratory, Argonne, IL 60439, USA

Correspondence e-mail: stern@phys.washington.edu

Received 31 October 2008
Accepted 15 February 2009

A new strategy is presented to reduce primary X-ray damage in macromolecular crystallography. The strategy is based on separating the diffracting and damaged regions as much as feasible. The source of the radiation damage to macromolecular crystals is from two primary mechanisms: the direct excitations of electrons by absorption, and inelastic scattering of the X-rays. The first produces photoelectrons with their accompanying Auger electrons from relaxation of the core hole and the second creates Compton electrons. The properties of these two mechanisms and calculations of primary X-ray damage quantify how to modify the spatial distribution of X-rays to reduce the deleterious effects of radiation damage. By focusing the incident X-rays into vertical stripes, it is estimated that the survival (the time during which quality diffraction data can be obtained with a given X-ray flux) of large crystals can be increased by at least a factor of 1.6, while for very small platelet crystals the survival can be increased by up to a factor of 14.

1. Introduction

One of the major limitations in macromolecular X-ray crystallography is radiation damage to the crystal. Experiments with third-generation synchrotrons have shown that the high flux of X-rays causes significant X-ray damage to macromolecular crystals during short exposures with a fully focused X-ray beam (Borek *et al.*, 2007; Sliz *et al.*, 2003; Teng & Moffat, 2002; Hedman *et al.*, 1985). This may result in many effects ranging from erroneous chemical interpretation of the structure to non-isomorphism of the data or failure to collect a complete data set and solve the structure (Borek *et al.*, 2007; Burmeister, 2000). The problem is highly amplified for structure-determination approaches that require multiple data sets, such as multiwavelength anomalous diffraction phasing (Schiltz *et al.*, 2004; Walsh *et al.*, 1999). The goal of this paper is to present and analyze a method that reduces deleterious radiation damage by reducing one of the components of the primary radiation damage.

The primary X-ray radiation damage is caused by electrons being directly excited in biological matter and solvent. Since for the X-ray energies used in macromolecular crystallography less than 15% of X-rays result in productive diffraction events and the remaining X-rays impart energy to biological crystals that results in damage, it is important to minimize the deleterious components (Gonzalez & Nave, 1994; Sliz *et al.*, 2003). The 'secondary' damage is caused by the highly reactive radiolytic species that propagate through the crystal, react with

macromolecules and cause further damage. Macromolecular crystals are particularly sensitive because the crystal-packing contacts are weak and can easily be disrupted. This is especially true for crystals of biologically important very large macromolecular assemblies such as viruses, membrane-protein and protein–nucleic acid complexes (Ravelli & Garman, 2006; Clemons *et al.*, 2001; Watowich *et al.*, 1995; Hope *et al.*, 1989). Radiation damage also limits data collection from small crystals and weakly diffracting crystals. Radiation damage caused by radiolytic products can be significantly diminished by collecting data from flash-frozen crystals at liquid-nitrogen or helium temperatures (Chinte *et al.*, 2007; Meents *et al.*, 2007; Sliz *et al.*, 2003; Hanson *et al.*, 2002; Garman, 2003). Data are now routinely collected from crystals kept at 100 K, significantly reducing secondary radiation damage and usually resulting in higher resolution and better quality data (Ravelli & Garman, 2006; Walsh *et al.*, 1999).

However, primary X-ray damage cannot at present be easily controlled and cryoprotected crystals are therefore still subject to radiation damage. Although radiation-induced changes are somewhat crystal-dependent, the overall radiation damage to cryopreserved protein crystals is in the first approximation proportional to the total dose (Borek *et al.*, 2007; Sliz *et al.*, 2003). The radiation damage limits the minimum quantity (crystal size) of the crystalline material needed to obtain a complete data set. Any improvement in controlling or reducing primary radiation damage would have a major impact on all of macromolecular X-ray crystallography, *e.g.* even a 30–40% improvement in the survival of crystals would improve the structure determination of very large macromolecular assemblies. As described below, by separating the X-ray-exposed and diffracting region from the damaged region, we expect to obtain at least a 60% improvement for large crystals and up to a 14-fold improvement for thin platelet crystals.

Although experimentally it is straightforward to determine the X-ray flux incident on a biological crystal, the portion of the flux that contributes to the damage is more difficult to determine and is usually determined by theoretical calculations. For these calculations we employ improved models/approximations of the interaction of X-rays with biological matter which more realistically describe radiation damage in macromolecular crystals (Kas *et al.*, 2007; Rehr *et al.*, 2006; Sorini *et al.*, 2006).

These improved calculations, denoted *FEFF*, are based on developments to explain the fine structure above X-ray absorption edges. The interaction of excited electrons with their environment is determined by a complex dielectric function $\varepsilon(\omega, \mathbf{p})$, where $\hbar\omega$ is the energy loss of the electron as it scatters with a momentum transfer $\mathbf{p}$. The theoretical approach of *FEFF* is based on *ab initio* calculations of the complex dielectric function $\varepsilon(\omega, 0)$ in the long-wavelength optical limit, together with extensions to finite $\mathbf{p}$. Thus, unlike most current approaches, the *FEFF* approach does not rely on empirical optical data which depend only on ω and are not available in many cases. *FEFF* calculations of $\varepsilon(\omega, \mathbf{p})$ are carried out using an all-electron real-space Green's function formalism which is more compatible with a locally varying complex dielectric function than are wavefunctions. All the significant factors are accounted for in *FEFF* calculations. We find that the results are consistent with semi-empirical approaches and experiment and have the additional potential to fill in the data range when experimental data are not available.

The primary interactions at photon energies appropriate for diffraction of biological crystals are of three types: (i) photon absorption with consequent photoelectron (PE) creation and Auger electron emission from resulting core hole excitations, (ii) inelastic (incoherent or Compton) photon scattering and (iii) elastic (coherent) scattering. Only (i) and (ii) cause radiation damage, while (iii) gives the diffraction signal. For larger crystals, essentially all of the energy produced in the primary processes will be deposited in the crystal. As discussed below, PE excitation dominates over Compton scattering for X-ray photon energies appropriate for crystallography. The quantity necessary to maximize for crystallography is L, the ratio of the diffraction signal to the amount of damage from energy deposition (the X-ray dose in the irradiated volume).

Although the rate of diffraction deterioration as a function of dose is most likely to depend on the particular type of biological crystal and the solvent composition, for any given crystal maximization of L results in the best diffraction signal. When crystal surface effects can be neglected and the sample is cold enough, L only depends on the primary interactions. Surface effects are only important if the electrons produced by interactions (i) and (ii) can escape from the irradiated crystal region either owing to the presence of an actual crystal surface or as a consequence of the X-ray beam not irradiating the whole crystal. Nave and Hill pointed out that in small enough crystals a significant amount of the energy of its primary electrons can escape and thus they may have fewer deleterious effects arising from radiation damage than large crystals that absorb all the primary damage (Nave & Hill, 2005). The use of a very small X-ray beam has recently been reported (Sanishvili *et al.*, 2008) and showed improved signal-to-noise ratios for data collected from small protein crystals using the mini-beam.

Another mechanism for energy from the primary interactions to escape from the crystal is as fluorescence photons from the relaxation of atoms excited by the photoelectron effect of (i). For low-Z elements such as S and below, the relaxation of these atomic excitations is dominated by Auger electron emissions whose energies are much smaller than those of the photoelectrons and thus the fluorescence loss can be neglected. The fluorescence mechanism is significant for intermediate-Z elements, but since (apart from a few exceptions, *e.g.* metal-storage proteins such as ferritin) intermediate-Z elements are a very small minority in proteins or nucleic acids they will initially be neglected and then discussed later in §3. The PE emitted in interaction (i) has the energy of the X-ray photon minus its binding energy in the atom. For the light elements of proteins and nucleic acids the binding energies are much smaller than X-ray photon energies and thus the PE will have an energy close to that of the photon. The Compton electrons excited in interaction (ii) will have

Table 1
List of parameters used in this paper.

Parameter	Description
ω_1	Angular frequency of X-ray photon
h	Planck's constant
$\hbar$	$h/2\pi$
m	Electron mass
c	Velocity of light
q	X-ray wavenumber = $2\pi/\lambda$
λ	X-ray wavelength
k	Photoelectron wavenumber
e	Electron charge

much smaller average energies, $\overline{E}_C$ = 783 eV for 20 keV photons (T. Fister, private communication). In general, $\overline{E}_C \simeq (\hbar\omega_1)^2/mc^2$, where $\hbar\omega_1$ is the X-ray photon energy and mc^2 = 511 keV, the electron rest mass energy. Table 1 lists the parameters used in this paper. By a judicious choice of the spatial distribution of X-rays, the L value can be increased over that for a uniform illumination of a larger crystal. In §2 we describe the strategy of how to reduce the effect of radiation damage and quantify the amount of reduction. It will be shown that for large crystals L can be increased by at least a factor of 1.6 and that for thin platelet crystals the increase could be up to a factor of 14.

2. Strategy

2.1. Qualitative considerations

The strategy for reducing the effect of radiation damage is to separate the crystal X-ray-exposed and diffracting region from the radiation-damaged region. This is possible because most of the primary damage is separated from diffracting atoms since most of the primary damage in macromolecular crystals is caused by PEs that typically deposit their damage several micrometres away. Fig. 1 illustrates the stopping power of PEs in a material composed of N atoms of density 1 g cm^{-3} as an approximation to biological matter. The stopping power is the average PE energy loss per unit distance by exciting electrons in the surrounding N atoms. Note that at initial PE energies of 10–20 keV the stopping power is small (1–2 keV μm^{-1}) and only becomes large near the end of the PE path where its energy has been reduced to a kiloelectron volt or so. The range of a PE as a function of its initial energy is presented in Fig. 2 in the continuous slowing-down approximation (CSDA), in which the electron is assumed to move in a straight line, losing only its average ionization loss as given by the stopping power. The two plots give the results of different calculations, with *FEFF* being the most modern and expected to be the most accurate. Note the 20% difference between the two theories. The actual distance the PE travels from its origin atom, the penetration distance, is expected to be less than its CSDA range because the PE does not travel in a straight line owing to scattering by interaction with the electrons of surrounding atoms.

For example, a Monte Carlo calculation (Nave & Hill, 2005) using the *CASINO* program (Hovington *et al.*, 1997) finds that a 20 keV PE with a CSDA range of 8 μm is not significantly transmitted through a plane perpendicular to the initial PE direction that is only 6 μm distant, *i.e.* its penetration distance is 6 μm or less. The additional important and pertinent property of the PE is its θ-dependence between the X-ray polarization and its initial emission direction of $\cos^2\theta$ in the dipole approximation. This occurs because the initial atom K-shell core state that dominates the PE process is 1s and by dipole-transition rules it can only be excited into a p-state which has the $\cos^2\theta$ distribution. However, the dipole approximation is less accurate for the more optimum energies of X-rays used in minimizing radiation damage in macromolecular crystals by our method described in §2.2. For our qualitative discussion here we can neglect this point.

The properties of the PE suggest the following strategy to reduce radiation damage in the diffracting region, as shown in

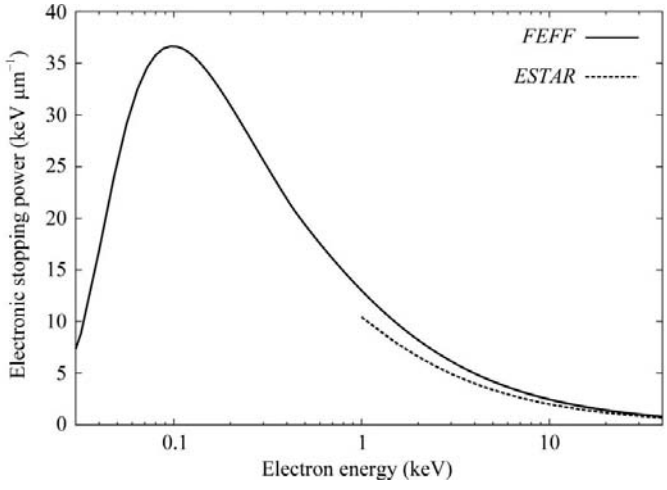

Figure 1
The stopping power of photoelectrons as a function of their energy for N atoms of density ρ = 1.0 g cm^{-3} calculated by *FEFF* and by *ESTAR* from NIST (Chantler *et al.*, 2005).The energy scale is log to the base 10. Since *ESTAR* data are not reliable below 1 keV their plot terminates there.

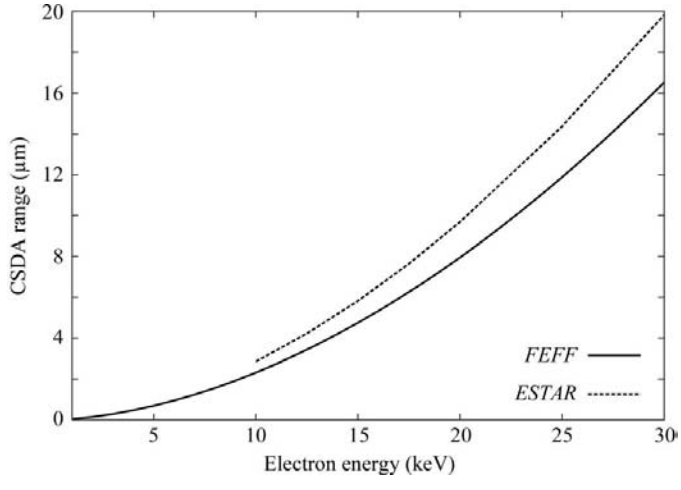

Figure 2
Range of electrons as a function of initial energy in N atoms of density ρ = 1.0 g cm^{-3} as calculated by *FEFF* and *ESTAR* (Chantler *et al.*, 2005) in the continuous slowing-down approximation (CSDA). Again, the *ESTAR* plots are terminated at a low limit because of unreliability.

Fig. 3. The rectangle is a crystal that is only irradiated with X-rays in the region of the black stripes. The polarization of synchrotron X-rays is horizontal, so that PEs are preferentially emitted in the horizontal directions. The distance d between the stripes is greater than the penetration distance of the PEs and the width of the stripes w is small so that the PEs lose only a small fraction of their energy within them. In this configuration most of the damage occurs between the stripes and all of the diffraction occurs within the stripes, which have reduced damage. This configuration satisfies our desire to separate the diffracting region from the damage. However, in order to obtain the same diffraction intensity as produced by a uniform irradiation of the crystal we need to increase the intensity in the stripes by the ratio of the crystal area to that of the stripes, namely $(w + d)/w$, neglecting end effects. Since the stopping power is nonlinearly weighted in the space between the stripes, it should be possible to reduce the damage with this configuration. Note that for 20 keV PEs, separating the stripes by $d = 6\,\mu m$ will prevent PEs from causing damage within neighboring stripes. However, as discussed below this may be an overly conservative value for d and a smaller value may be sufficient.

Small crystals and thin platelets deserve special attention because surface effects are large, suggesting that greater improvements in the diffraction signal-to-damage ratio are possible. As shown in Fig. 4, the strategy here will be to focus the beam to one or a few stripes perpendicular to the polarization vector and to align the crystal so that the beam enters the crystal through its narrow side and propagates parallel to its large faces. In this way the mother liquid adjacent to the large faces of the crystal will not be illuminated and few damaging photoelectrons will be produced in the mother liquid. The damage produced by photoelectrons excited near the narrow edges will be relatively small. In order for the sample to remain in this favorable configuration as it is rotated, the rotation axis has to be parallel to the polarization vector in Fig. 4. The next section presents quantitative calculations to support the qualitative conclusions.

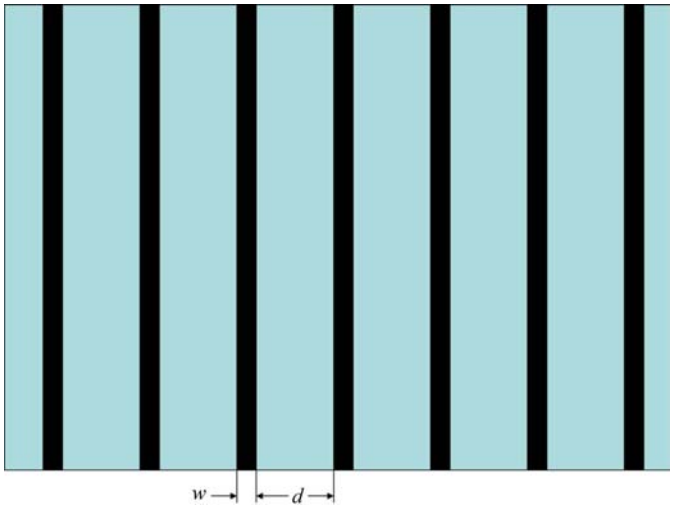

Figure 3
A rectangular crystal irradiated with X-rays focused to impinge on only the regions highlighted by the black stripes of width w and separated by non-radiated regions of width d.

2.2. Quantitative calculation

2.2.1. Large crystals. The quantitative calculation is based on PE, Compton scattering and diffraction cross-section values given in the McMaster tables (McMaster *et al.*, 1969), supplemented by calculations of the energy imparted to the Compton electrons. Justification for using the McMaster tables is shown in Fig. 5. Note that the McMaster curve agrees with the *FEFF* curve and that of the FFAST method of calculating the PE cross-sections, giving confidence that the McMaster cross-sections are reasonably accurate.

Our initial qualitative discussion in the previous section only considered the damage caused by the photoelectrons and neglected three other contributions: the emission of low-energy Auger electrons owing to the relaxation of the X-ray-excited atoms to their ground states, the energy deposited by Compton electrons and the $\cos^2\theta$ angular dependence of the PEs, which increases their effective path length inside the stripe by a factor of 1.5. Even though for uniform illumination the total energy deposition from the first two contributions is much smaller than that of the PEs, they have an enhanced detrimental effect in our case since their energy absorption is localized in the diffracting region while the PE damage is concentrated outside of the stripes.

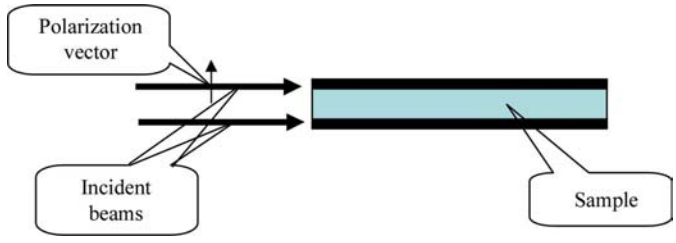

Figure 4
Schematic diagram for X-rays illuminating thin (for example 8 μm) platelet crystals.

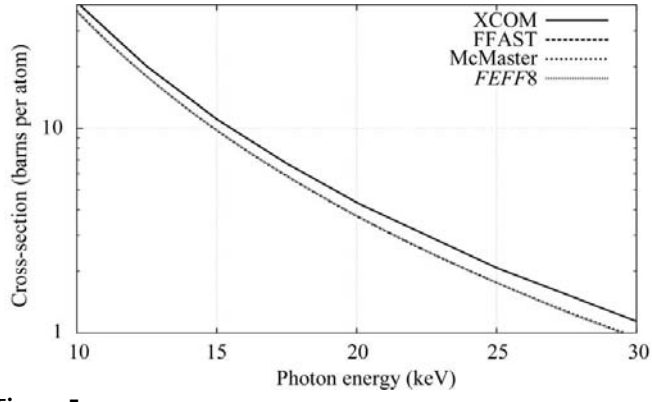

Figure 5
Calculated photoelectric cross-sections of C atoms in the dipole approximation as a function of X-ray energy. Note that the FFAST (Chantler *et al.*, 2005), McMaster (McMaster *et al.*, 1969) and our *FEFF*8 curves overlap and are not distinguishable, while the XCOM (Berger *et al.*, 1990) curve is above the other three.

The $\cos^2\theta$ dependence is valid in the dipole approximation, which requires $qa_z << 1$, where the X-ray wavenumber $q = 2\pi/\lambda$, a_Z is the radius of the 1*s* core electron state for an atom of atomic number Z and λ is the X-ray wavelength. The 1*s* core state is excited to an unbound *p* state. At 20 keV, $qa_Z = 1.45$, 1.22 and 1.06 for C, N and O atoms, respectively, indicating that the dipole approximation requires corrections. In particular, the usual next-order quadrupole correction (see, for example, Trzhaskovskaya *et al.*, 2006) is no longer sufficient since higher multipoles are significant. In spite of this, at X-ray energies employed for macromolecular crystallography which are much higher than the 1*s* state binding energy of C, N and O atoms the $\cos^2\theta$ dependence and dipole value for cross-sections of the PEs are still good approximations, as shown in Appendix *A* where the sum over all multipoles is performed. Although ~20 keV X-rays are higher energy photons than are typically employed in macromolecular crystallography they are chosen here because they have less energy loss in the diffracting stripes (Fig. 1) and are still accessible at many macromolecular crystallography synchrotron beamlines. Another advantage of using the higher energy of 20 keV is that its penetration distance is within 6 μm, so the spacing of stripes in Fig. 3 can be large enough to ease the fabrication of the required separate focusing element for each stripe. A recent publication (Shimizu *et al.*, 2007) has found that the quality of diffraction data as a function of X-ray energy did not vary significantly over the energy range 6.5–33 keV, justifying the use of our different criteria for choosing the X-ray energy.

The values from the McMaster table for 20 keV X-rays were applied to a typical protein crystal which contains about 50% solvent consisting of water molecules and 50% protein matter, with a density of 1.17 g cm^{-3}. Its atomic composition is

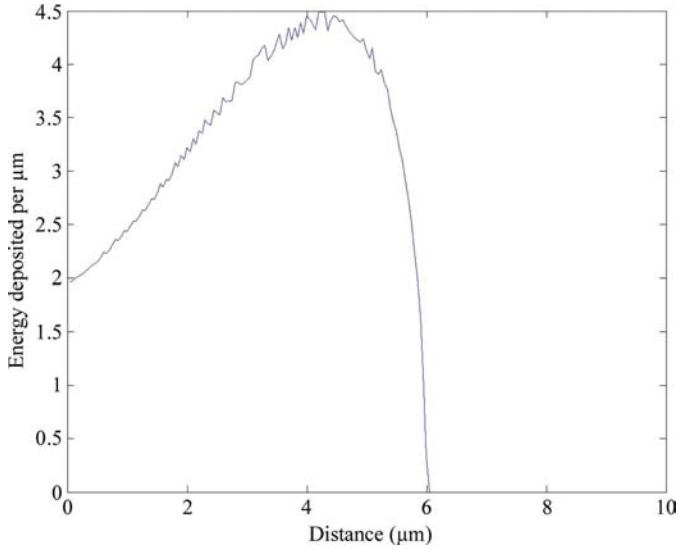

Figure 6
The angular-averaged energy in keV per micrometre deposited by a photoelectron as a function of *x*, the distance normal to the stripe plane. The stripe plane from 0 to 1 μm is uniformly irradiated by 20 keV X-rays. This calculation takes into account both the fact that the photoelectron does not propagate in a straight line and its angular distribution relative to the horizontal X-ray polarization.

Table 2
Dose per average atom in a large bio-crystal (b/a is barns per average atom).

Mechanism	Dose (keV b/a)	Dose relative to PE dose
Photoelectrons	79.2	1.0
Auger electrons	2.00	0.025
Compton electrons	1.54	0.019
Total	82.7	1.044

$C_{1818}N_{420}O_{2673}H_{7286}S_{25}$. This typical protein example was obtained (Nave & Hill, 2005) from a bio-information toolkit at http://www.mathworks.com/access/helpdesk/help/toolbox/bioinfo/a10481870091.html with atoms of 1856 molecules of water added. The cross-sections of 20 keV X-rays were found for the three processes (i) PE, (ii) inelastic (Compton electrons) and (iii) elastic (diffraction) scattering. The Auger electrons are produced when the PEs are created and thus have the same cross-section. These various cross-sections are found for each atom type. Next, the cross-sections of the three processes were multiplied by their respective energy losses to obtain their contribution to the dose. The doses were then averaged by weighting by their percentage in the crystal, obtaining the average dose per atom per X-ray photon. In the calculations the effect of the S atoms was small compared with the rest of the atoms and is neglected.

The dose produced by an average atom in our large typical bio-crystal uniformly illuminated by 20 keV X-rays is distributed among the various mechanisms in the proportion given in Table 2. Note that the PE dose dominates in a uniformly irradiated large crystal. Since the dose from a PE plus that of its Auger electrons is 20 keV when a photon is absorbed, the total dose from all processes, in which on average one PE is created, is $(1.044/1.025) \times 20.0 = 20.37$ keV (the Compton dose is 0.37 keV).

In a stripe of Fig. 3 with width $w = 2x$ the average path length of a photoelectron moving horizontally along the polarization direction of an X-ray produced using synchrotron radiation is *x*. However, taking into account the $\cos^2\theta$ angular dependence and the subtended solid angle proportional to $\sin\theta$, the average path length becomes $1.5x$. From Fig. 1, the stopping power of an ~20 keV PE inside the stripe is 1.5 keV μm^{-1}. For such energetic electrons one expects that to a good approximation the PE will move in a straight line and lose on average $\Delta E_{PE} = 1.5 \times 1.5x = 2.25x$ keV in a stripe. Here, we can understand that setting the spacing d to 6 μm, the penetration distance of 20 keV PEs emitted along $\theta = 0$, is too conservative since the solid angle there is zero, while the average angle of PE emission is $\theta_a = \sin^{-1}(1/1.5) = 48.2^\circ$. The penetration distance of a PE at this average angle projected onto the horizontal axis is $2d/3$. Unfortunately, the situation is not so simple since the actual path of a PE is scattered and spread about its initial emitted angle. For this reason, we calculate the optimum condition for reducing the damage for values of both $d = 5$ and 6 μm to suggest the effect of a shorter effective d. In any case $d = 6$ μm is a lower limit to the predicted improvement factor. The PE excitation also deposits within the stripe about 0.49 keV through the Auger electrons

and an additional 0.37 keV comes from Compton electrons. However, to obtain the same diffraction intensity from the stripes as in a uniformly irradiated sample its intensity must be increased by the ratio of the crystal area divided by the area of the stripes, *i.e.* by $(d + 2x)/2x$. Thus, under the same diffraction intensity conditions the ratio of the dose in the uniformly irradiated sample to the stripe-focused sample is

$$R(x, d) = 20.37/[(2.25x + 0.49 + 0.37)(d + 2x)(2x)^{-1}]. \quad (1)$$

Differentiating $R(x, d)$ with respect to x and setting it to zero gives a maximum value of $R(1.0, 6) = 1.6$ and $R(1.0, 5) = 1.8$. Thus, in both cases $x = 1.0$ µm (the stripe width is 2 µm) and the survival of the crystal is enhanced by 1.6 and 1.8 for $d = 6$ and 5 µm, respectively. The center-to-center distance between the stripes is 8 and 7 µm, respectively. This calculation suggests that the survival of large bio-crystals can be increased by at least 60%.

Fig. 6 shows a plot of a numerical calculation of the distribution of the PE damage that occurs from a single stripe in large crystals if the effective penetration distance is 6 µm. The calculation accounts for the PE scattering and its $\cos^2\theta$ distribution. Fig. 6 illustrates how the damage induced by PEs is mostly concentrated between the stripes. In this plot, X-rays uniformly irradiate only the stripe in the range 0 –1 µm where the PEs originate. Since the plot is symmetric about the y axis, in the plot the $-x$ values are folded over the $+x$ values in the angle averaging to double the dose values. The total dose in the region between the stripes is given by the area under the curve in the range from 1 to 6 µm, while the dose in the stripe is the area from 0 to 1 µm and is equal to 2.25 keV, which is in agreement with that in the above paragraph of $2.25x$ for $x = 1$ µm.

2.2.2. Thin platelets. Thin platelets will be illuminated in the way shown in Fig. 4. For 20 keV X-rays, the center-to-center spacing between the line-focused X-ray beams will always be 8 µm. The number and size of the foci has been changed so as to optimize the improvement factor for each sample thickness. The results are shown in Fig. 7. In general, the fact that two of the focused beams can be at the two sides of the sample means that the photoelectrons excited by these beams deposit about half of their energy outside the sample, thus increasing the improvement factor from 1.6 at large thicknesses to about 2 at 17 µm and to 2.6 at 8 µm. At this latter thickness the sample is illuminated by two stripes 1 µm wide, each just inside the two surfaces of the sample. At thicknesses below 6 µm the sample is illuminated by just one focused beam. For each sample thickness the focused stripe width was adjusted to provide the optimal improvement factor. It turns out that below 5 µm it is best to illuminate the whole sample with one stripe refocused to a width equal to the platelet thickness. The minimum in the improvement factor at 6 µm arises from the fact that the sample can no longer be illuminated by two beams separated by 6 µm. The improvement factor may be increased by reducing the X-ray photon energy because the distance between the focused beams can be smaller than 6 µm, allowing two focused beams to be used.

3. Discussion and conclusions

Nave & Hill (2005) suggested that the surface effect in very small crystals where a significant number of primary electrons escape the crystal can reduce the deleterious effects of primary radiation damage on the diffraction signal. We show that this indeed is the case by quantitatively estimating how large the reduction can be. A recent publication (Cowan & Nave, 2008) published after our manuscript was written has improved on Nave & Hill (2005) by adding the losses arising from Compton scattering and Auger electron emission from resulting core hole excitations. The main differences from our paper are not adding spatial distribution to the X-rays, being limited to very small crystals, and using the old less accurate calculations as shown in Figs. 1 and 2.

Inspired by Nave & Hill (2005), a recent publication (Moukhametzianov *et al.*, 2008) described a technically very impressive diffraction result on a small crystal of 20 µm^3 volume by focusing the X-ray beam to a 1 µm point. Here, we have pointed out that one can do better by focusing in a vertical line (stripe). The authors overcame the high dosing at the 1 µm focal point by introducing a small intentional displacement of the focus (2–5 µm) off the vertical rotation axis, which in effect distributed the exposure along the surface of a cylinder about that axis that covered a circular region in a horizontal plane. In this manner, they were able to obtain data to 1.5 Å resolution. Although at each angular value a diffraction pattern to 1.5 Å resolution was possible, to cover the >180° angular spread for a complete data set required irradiation of a crystal of more than 150 µm^3 in volume. Their data were obtained with 13 keV photons, which have a PE CSDA range of 3.5 µm that, after scattering, could somewhat damage the surrounding circular region used for the later measurements. Our strategy should perform even better, since the planar stripes produce less collateral damage than a circular one, especially with the higher energy 20 keV photons.

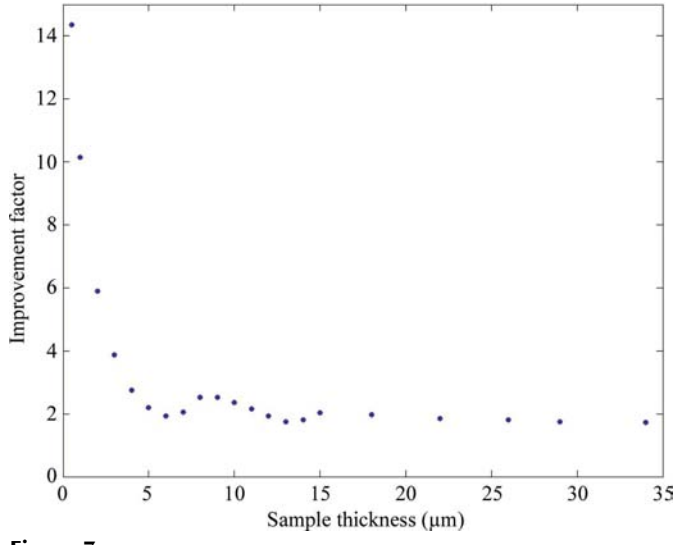

Figure 7
The improvement factor for thin platelets as a function of sample thickness. Below 15 µm sample thickness the points are spaced at 1 µm intervals.

In particular, we calculate that in thin platelets the survival can increase by a factor of up to 14.

In addition, we show that in large crystals it ought to be possible to reduce the deleterious effects of radiation damage on the diffraction signal by a factor of at least 1.6. In the case of our method, the size of 'large' depends on the X-ray energy, since the crystal should have dimensions in the direction perpendicular to the irradiating X-rays significantly larger than twice the PE penetration depth. From Fig. 7 it can be noted that 'large' is greater than about 30 μm for 20 keV photons. For 13 keV X-rays 'large' is greater then about 13 μm. For large crystals greater than about 35 μm there is little advantage to our method since other strategies can be used for data collection that will achieve good results with less effort, *e.g.* translating or miscentering the crystal. Of course, combining these same strategies with our method will still give the 1.6-fold improvement. The 35 μm size is twice the thickness in Fig. 7, where the improvement factor is 2.

In both large and small crystals the reduction in damage occurs by separating the X-ray-irradiated region from that in which most of the damage occurs. In the case of large crystals this is accomplished by focusing the X-ray beam from a uniform distribution to one where the X-rays are concentrated into a series of sheets or stripes whose planes are oriented vertically as shown in Fig. 3 and are separated by a distance within which most of the damage is concentrated (Fig. 6). Since the X-rays from synchrotron sources are polarized in the horizontal direction they cause the photoelectrons (PEs), the main source of primary radiation damage, to be preferentially emitted in the direction away from the stripes.

In the large crystal case coming to the conclusion of a reduction in deleterious effects is not as obvious as it is for the small crystal case because there are now competing effects that require a quantitative calculation and a judicial choice of parameters to end up with a significant improvement. Separating the diffracting region from the damaging primary electrons requires concentrating the X-rays into smaller stripe regions, which increases the production of all of the primary damaging processes in that region. The diffraction process in the region is also increased by the same ratio, but as the overall diffraction signal is not increased it is not obvious that damage is truly decreased, requiring judicious choices of how best to focus the X-rays and of what energy of X-rays to use. In contrast, in the small crystal case there is only a gain in the diffraction signal by focusing the X-rays onto the crystal, eliminating PE damage from the mother-liquid coating while still losing damaging electrons, so the benefit is intuitively obvious.

Our discussion has considered bio-crystals containing only light atoms. Heavy atoms will be a source of much denser damage concentrated about their sites for the following reasons: the cross-section for PE creation is much greater, the PE energy is less, with a concomitantly smaller CSDA range, and the cascade of low-energy Auger electrons from the relaxation of the excited core hole deposits much greater energy locally. As an example, for Se atoms and 20 keV X-rays the PE energy is 7.3 keV with a CSDA range of 1.6 μm and its cross-section is 800 times greater (!) than that of an average protein light atom. In addition, over half of its excited core energy of 13.7 keV relaxes by creating many low-energy Auger electrons that deposit their energies in the close vicinity of the Se site. The remaining core hole energy relaxes by emitting fluorescence X-rays, consisting mostly of 11.2 and 11.5 keV photons that are likely to escape the crystal without interacting. These calculations caution that care should be taken to not overdose locally at heavy-atom sites when phasing data are obtained.

In the course of making our damage estimates, we include primary damage mechanisms that have previously been neglected. These are the Auger electrons emitted from the atoms excited by PE emission and the Compton electrons excited in incoherent scattering of the X-rays. These electrons have much lower energies than those of the PEs and deposit their energies locally in the region in which they originate. In uniform illumination of large crystals the damage caused by these two mechanisms is a small addition to that produced by the PEs. However, the new mechanisms make a more significant contribution to the damage when X-rays are focused into small regions and need to be included in this case. Another new result was to point out that the dipole approximation is not valid at the higher X-ray energies required to separate the damaged regions from the irradiated regions and that the quadrupole correction is not sufficient to solve the problem. Fortunately, at the required higher X-ray energies a new parameter determines the properties of PE emission which results in only small changes in the PE electron behavior from that of the dipole approximation as shown in Appendix *A* by summing over all multipoles. Thus, it was possible to use the results of McMaster tables, which are based on the dipole approximation, to calculate the required properties of the PEs and for other cross-sections which are not dependent on the dipole approximation.

In conclusion, taking advantage of the methods described here to reduce the deleterious effects of X-ray damage requires new X-ray spatial distributions and the use of higher X-ray energies than are usually employed. This introduces new technical challenges to synchrotron macromolecular beamlines, but they are not insurmountable. The technology to produce the vertical stripes of X-rays is now available by using refractive X-ray lenses (Stein *et al.*, 2003; Evans-Lutterodt *et al.*, 2003, 2004). Another adjustment that is necessary is the alignment of the stripes accurately perpendicular to the rotation axis so that the width of the irradiated crystal at stripes remains 2 μm within 0.1 μm, *e.g.* for a 100 μm high stripe the alignment should be within a milliradian (0.057°).

APPENDIX *A*

Here, we develop a more accurate expression for the PE cross-section and angular distribution that goes beyond the dipole approximation in the limit where the X-ray photon energies are much greater than the 1*s* core binding energy, as is the case for the low-*Z* atoms of biological matter. The interaction of an

X-ray with the 1*s* core is proportional to the square of the matrix element

$$M = \langle 0|e\mathbf{A}\cdot\mathbf{p}|\exp[i(\mathbf{k}\cdot\mathbf{r})]\rangle, \quad (2)$$

where $\langle 0| = \Psi_0(r)$ is the 1*s* core state, $\mathbf{A} = \mathbf{A}_0\exp(i\mathbf{q}\cdot\mathbf{r})$ is the X-ray vector potential, $\mathbf{p}$ is the momentum operator, $\mathbf{q}$ is the wavenumber of the X-ray photon and $\mathbf{k}$ is the PE wavevector. Explicitly, the matrix element has the form

$$M(\mathbf{q},\mathbf{k}) = e\hbar\mathbf{A}_0\cdot\mathbf{k}\int\Psi_0(\mathbf{r})\exp[i(\mathbf{k}+\mathbf{q})\cdot\mathbf{r}]\,\mathrm{d}^3r. \quad (3)$$

Since $\Psi_0(\mathbf{r})$ is spherically symmetric, the integral in (3) only depends on $|\mathbf{k}+\mathbf{q}| = (k^2+q^2+2\mathbf{k}\cdot\mathbf{q})^{1/2}$. According to the WKB approximation, in the region where the PE wavefunction overlaps the core state $(\hbar k)^2/2m = \hbar\omega = \hbar qc$, *i.e.* the PE has the same energy as the X-ray photon. The k of the nonrelativistic 20 keV PE is much greater than the photon q, allowing an expansion in q/k. To first order in q/k, $|\mathbf{k}+\mathbf{q}| \simeq (k^2+2\mathbf{k}\cdot\mathbf{q})^{1/2} \simeq k[1+(k_xq/k^2)]$ and consequently, by a Taylor series expansion about the k value of $q = 0$, the absolute squared value of the matrix element is given by

$$|M|^2 = (e\hbar\mathbf{A}_0\cdot\mathbf{k})^2S_0(k)\left\{1+\frac{\mathbf{k}\cdot\mathbf{q}}{k}\frac{\partial}{\partial k}\ln[S_0(k)]\right\}, \quad (4)$$

where

$$S_0(k) = \left|\int\Psi_0(r)\exp[i(\mathbf{k}+\mathbf{q})\cdot\mathbf{r}]\,\mathrm{d}^3r\right|^2. \quad (5)$$

Note that (5) contains all multipole contributions.

Assuming the X-ray beam is propagating in the x direction and is polarized in the z direction,

$$|M|^2 = |M_d|^2\left\{1+q\sin(\theta)\cos(\varphi)\frac{\partial}{\partial k}\ln[S_0(k)]\right\} \quad (6)$$

to first order in q/k and

$$|M_d|^2 = (e\hbar A_0k)^2\cos^2(\theta)S_0(k) \quad (7)$$

is the square of the dipole matrix element. Here, θ is the angle between the X-ray polarization (which is along the positive z axis) and the PE emission direction and $\mathbf{k}$ is the wavevector of the PE which is emitted in direction (θ,φ), where (θ,φ) are the usual spherical angular coordinates. Performing the integrals and derivative of (6) and (7) gives the cross-section for PE emission

$$\sigma(\theta,\varphi,q,k) = \sigma_d(\theta,k)\left[1-\frac{4k}{(k^2+a_Z^{-2})}q\sin\theta\cos\varphi\right]. \quad (8)$$

Here, a_Z is the radius of the 1*s* state of an atom of nuclear charge $Z|e|$ and $\sigma_d(\theta,k) \propto \omega^{-1}(k^2+a_Z^{-2})^{-2}\cos^2\theta$ is the dipole cross-section for PE emission.

For incident X-rays of energy $\hbar\omega_1 = 20$ keV, $q = \omega/c$ and the k of a PE is given by $[(\hbar k)^2/2m] = 20$ keV, giving $q/k = 0.14$. For 13 keV, which is within the energy range for which most structural biology synchrotron beamlines are currently optimized, $q/k = 0.11$. The general expression $q/k = 0.0313(\hbar\omega_1)^{1/2}$, where the photon energy $\hbar\omega_1$ is in keV units, applies for all nonrelativistic PE energies. For the correction term to be a good approximation, $(q/k)\sin\theta\cos\varphi$, the series-expansion parameter, should be small compared with 1, which is the case up to at least 100 keV; this is much superior to the standard quadrupole correction approximation. Note that the total PE cross-section integrated over all angles is not changed to first order in the expansion parameter since the integration over φ is zero; only the angular distribution is changed by a small amount.

The correction term in (5) distorts the two lobes of the dipole $\cos^2\theta$ angular distribution from being symmetric about the z axis by bowing the symmetry line of each to negative x, leaving the symmetry line pinned to three original points on the z axis corresponding to $\theta = 0$, π, where $\sin\theta = 0$, and $\theta = \pi/2$, where $\cos^2\theta = 0$. Since $\mathbf{q}$ is directed in the positive x direction, the net emission of PEs is in the opposite x direction owing to this distortion. Note that the correction term is zero in the zy plane where $\cos\varphi = 0$, while it is maximized in the zx plane where $\cos\varphi = \pm1$. For our estimates based on McMaster table calculations, we assume the dipole approximation. Neglecting the corrections in the PE cross-section introduces errors of the order of 1% (probably within the accuracy of the McMaster dipole values), while the effect of neglect of the correction in the PE angular distribution is also small, changing its average angle from the polarization direction by a small amount but still maintaining it predominately along the polarization direction.

We gratefully acknowledge the support of NSF grant No. 0650547 (EAS) for this research and the US Department of Energy, Office of Biological and Environmental Research under contract DE-AC02-06CH11357 (AJ). EAS is grateful to Dr Robert Fischetti for a discussion that inspired the writing of this publication.

References

Berger, M. J., Hubbell, J. H., Seltzer, S. M., Chang, J., Coursey, J. S., Sukumar, R. & Zucker, D. S. (1990). *XCOM: Photon Cross Sections Database.* http://physics.nist.gov/PhysRefData/Xcom/Text/XCOM.html.

Burmeister, W. P. (2000). *Acta Cryst.* D**56**, 328–341.

Borek, D., Ginell, S. L., Cymborowski, M., Minor, W. & Otwinowski, Z. (2007). *J. Synchrotron Rad.* **14**, 24–33.

Chantler, C. T., Olsen, K., Dragoset, R. A., Chang, J., Kishore, A. R., Kotochigova, S. A. & Zucker, D. S. (2005). *X-ray Form Factor, Attenuation and Scattering Tables.* http://physics.nist.gov/PhysRefData/FFast/html/form.html.

Chinte, U., Shah, B., Chen, Y.-S., Pinkerton, A. A., Schall, C. A. & Hanson, B. L. (2007). *Acta Cryst.* D**63**, 486–492.

Clemons, W. M. Jr, Brodersen, D. E., McCutcheon, J. P., May, J. L., Carter, A. P., Morgan-Warren, R. J., Wimberly, B. T. & Ramakrishnan, V. (2001). *J. Mol. Biol.* **310**, 827–843.

Cowan, J. A. & Nave, C. (2008). *J. Synchrotron Rad.* **15**, 458–462.

Evans-Lutterodt, K., Ablett, J. M., Stein, A., Tennant, D. M., Klemens, F. & Taylor, A. (2004). *Proc. SPIE*, **5539**, 73–79.

Evans-Lutterodt, K., Stein, A., Ablett, J. M., Kao, C. C., Tennant, D., Klemens, F., Taylor, A., Jacobsen, A. C., Gammel, P., Ustin, S., Bogart, G. & Ocola, L. (2003). *Synchrotron. Radiat. News*, **16**, 60–63.

Garman, E. (2003). *Curr. Opin. Struct. Biol.* **13**, 545–551.

Gonzalez, A. & Nave, C. (1994). *Acta Cryst.* D**50**, 874–877.

Hanson, B. L., Harp, J. M., Kirschbaum, K., Schall, C. A., DeWitt, K., Howard, A., Pinkerton, A. A. & Bunick, G. J. (2002). *J. Synchrotron Rad.* **9**, 375–381.

Hedman, B., Hodgson, K. O., Helliwell, J. R., Liddington, R. & Papiz, M. Z. (1985). *Proc. Natl Acad. Sci. USA*, **82**, 7604–7607.
Hope, H., Frolow, F., von Böhlen, K., Makowski, I., Kratky, C., Halfon, Y., Danz, H., Webster, P., Bartels, K. S., Wittmann, H. G. & Yonath, A. (1989). *Acta Cryst.* B**45**, 190–199.
Hovington, P., Drouin, D. & Gauvin, R. (1997). *Scanning*, **19**, 1–14.
Kas, J. J., Sorini, A. P., Prange, M. P., Cambell, L. W., Soininen, J. A. & Rehr, J. J. (2007). *Phys. Rev. B*, **76**, 195116.
McMaster, W. H., Kerr Del Grande, N., Mallett, J. H. & Hubbel, J. H. (1969). *Periodic Table: X-ray Properties.* http://www.csrri.iit.edu/periodic-table.html.
Meents, A., Wagner, A., Schneider, R., Pradervand, C., Pohl, E. & Schulze-Briese, C. (2007). *Acta Cryst.* D**63**, 302–309.
Moukhametzianov, R., Burghammer, M., Edwards, P. C., Petitdemange, S., Popov, D., Fransen, M., McMullan, G., Schertler, G. F. X. & Riekel, C. (2008). *Acta Cryst.* D**64**, 158–166.
Nave, C. & Hill, M. A. (2005). *J. Synchrotron Rad.* **12**, 299–303.
Ravelli, R. B. & Garman, E. F. (2006). *Curr. Opin. Struct. Biol.* **16**, 624–629.
Rehr, J. J., Kas, J. J., Prange, M. P., Sorini, A. P., Campbell, L. W. & Vila, F. D. (2006). *Proceedings of the X-Ray Absorption Fine Structure – XAFS13: 13th International Conference*, edited by B. Hedman & P. Pianetta, pp. 85–88. Melville: American Institute of Physics.
Sanishvili, R., Nagarajan, V., Yoder, D., Becker, M., Xu, S., Corcoran, S., Akey, D. L., Smith, J. L. & Fischetti, R. F. (2008). *Acta Cryst.* D**64**, 425–435.
Schiltz, M., Dumas, P., Ennifar, E., Flensburg, C., Paciorek, W., Vonrhein, C. & Bricogne, G. (2004). *Acta Cryst.* D**60**, 1024–1031.
Shimizu, N., Hirata, K., Hasegawa, K., Ueno, G. & Yamamoto, M. (2007). *J. Synchrotron Rad.* **14**, 4–10.
Sliz, P., Harrison, S. C. & Rosenbaum, G. (2003). *Structure*, **11**, 13–19.
Sorini, A. P., Kas, J. J., Rehr, J. J., Prange, M. P. & Levine, Z. H. (2006). *Phys. Rev. B*, **74**, 165111.
Stein, A., Jacobsen, C., Evans-Lutterodt, K., Tennant, D. M., Bogart, G., Klemens, F., Ocola, L. E., Choi, B. J. & Sreenivasan, S. V. (2003). *J. Vac. Sci. Technol. B*, **21**, 214–219.
Teng, T.-Y. & Moffat, K. (2002). *J. Synchrotron Rad.* **9**, 198–201.
Trzhaskovskaya, M. B., Nikulin, V. K., Nefedov, V. I. & Yarzhemsky, V. G. (2006). *At. Data Nucl. Data Tables*, **92**, 245–304.
Watowich, S. J., Skehel, J. J. & Wiley, D. C. (1995). *Acta Cryst.* D**51**, 7–12.
Walsh, M. A., Evans, G., Sanishvili, R., Dementieva, I. & Joachimiak, A. (1999). *Acta Cryst.* D**55**, 1726–1732.